

Scanning Tunneling Spectroscopy

Harold J.W. Zandvliet and Arie van Houselt

Physical Aspects of Nanoelectronics and the MESA+ Institute for Nanotechnology, University of Twente, 7500 AE Enschede, The Netherlands; email: h.j.w.zandvliet@utwente.nl

Annu. Rev. Anal. Chem. 2009. 2:37–55

First published online as a Review in Advance on November 21, 2008

The *Annual Review of Analytical Chemistry* is online at anchem.annualreviews.org

This article's doi:
10.1146/annurev-anchem-060908-155213

Copyright © 2009 by Annual Reviews.
All rights reserved

1936-1327/09/0719-0037\$20.00

Key Words

scanning probe microscopy, surfaces, single-electron tunneling, thermodynamics

Abstract

The scanning tunneling microscope (STM) has revolutionized our ability to explore and manipulate atomic-scale solid surfaces. In addition to its unparalleled spatial power, the STM can study dynamical processes, such as molecular conformational changes, by recording current traces as a function of time. It can also be employed to measure the physical properties of molecules or nanostructures down to the atomic scale. Combining STM imaging with measurement of current–voltage (I – V) characteristics [i.e., scanning tunneling spectroscopy (STS)] at similar resolution makes it possible to obtain a detailed map of the electronic structure of a surface. For many years, STM lacked chemical specificity; however, the recent development of STM–IETS (inelastic electron tunneling spectroscopy) has allowed us to measure the vibrational spectrum of a single molecule. This review introduces and illustrates these recent developments with a few simple scholarly examples.

STM: scanning tunneling microscopy

TRSTM: time-resolved scanning tunneling microscopy

LDOS: local density of states

SET: single-electron tunneling

IETS: inelastic electron tunneling spectroscopy

1. INTRODUCTION

Until the 1930s, microscopy relied on optical methods with a spatial resolution that was limited by Abbé's diffraction limit, i.e., $\sim 1 \mu\text{m}$. To overcome this hurdle, Ernst Ruska (1) developed a novel type of microscopy that uses high-energy electrons. Despite the strongly enhanced spatial resolution of Ruska's electron microscope, it was Erwin Müller (2) who obtained the first atomically resolved images using field ion microscopy. However, the major breakthrough in the field of microscopy was the invention of the scanning tunneling microscope (STM) in the early 1980s by Binnig & Rohrer (3). In the STM, a metallic tip is brought so close to the sample that the wave functions of tip and sample begin to overlap. Upon application of a small voltage (V) difference between tip and sample, a tunneling current flows from tip to surface or vice versa. This tunneling current depends strongly on the overlap of the wave functions of tip and surface. In the low bias range, the tunneling current (I) can be approximated by

$$I \propto \frac{CV}{z} e^{-2\kappa z},$$

where z is the separation between substrate and tip, C is a constant, and κ is the inverse decay length (4, 5). In the standard imaging process, the tip scans over the surface and a feedback system attempts to keep the tunneling current constant by varying the substrate-tip distance, z . This frequently used mode of imaging is known as constant current topography mode. The z -piezo regulation voltage is recorded during scanning and is usually represented by a level gray image. The bright areas correspond to protrusions on the substrate and the darker ones to depressions. For very flat substrates and small scanning areas, it is possible to measure the tunneling current during scanning while keeping the height constant. This mode is referred to as constant height topography.

During the past 25 years, the unparalleled spatial power of the STM to image and manipulate atoms and molecules has received considerable attention in a number of excellent review papers (6, 7). Since the invention of the STM, there has been an ongoing effort not only to improve the already existing spectroscopic modes of the STM, but also to develop new ones.

Here we review a number of spectroscopic modes of the STM, which we illustrate with a few scholarly examples. By no means have we attempted to review all the developed spectroscopic modes of the STM; instead, we focus on a limited set of methods that we believe are of particular interest for the chemical community.

We begin with perhaps the least well-known spectroscopic mode, namely time-resolved scanning tunneling microscopy (TRSTM). The two examples presented in the following section reveal that this mode can operate in both closed-loop and open-loop configurations. Thereafter, we discuss the well-known I - V spectroscopy technique. The dI/dV signal can provide information about the local density of states (LDOS) of the surface, the spatial variation of electronic wave functions, and single-electron tunneling (SET) phenomena. Subsequently, we address the I - z spectroscopic mode, which can provide information on the work function and the inverse decay length of the wave functions that penetrate into the vacuum.

Finally, we discuss the most recent (and for chemists probably the most appealing) spectroscopic technique, namely inelastic electron tunneling spectroscopy (IETS).

Until recently, a major drawback of STM was its lack of chemical sensitivity. However, in the late 1990s Wilson Ho and coworkers (8) demonstrated that chemical analysis with the STM is possible by probing the electrons that tunnel inelastically. This technique can probe the vibrational modes of a molecule down to the scale of a single bond and can thus serve as a fingerprinting technique for chemical analysis.

2. TIME-RESOLVED SCANNING TUNNELING SPECTROSCOPY

2.1. Closed-Loop Spectroscopy

An important limitation of the STM is its poor time resolution. Recording an image with a fast-scanning STM typically takes from <1 s to 20–30 s for a standard STM. The cut-off frequency of the feedback loop is usually on the order of a few kilohertz, which implies that the dynamic processes that occur on a timescale of a millisecond or less are averaged out in the scanning process.

In 1996, Swartzentruber et al. (9) showed that the STM can be used to study dynamical processes with a time resolution in the millisecond range. They monitored the rotation of an adsorbed silicon dimer on a dimerized Si(001) surface by recording *z*-piezo voltage traces as a function of time. The two stable configurations, which we term A and B, respectively, have a different *z*-feedback position because of their electronic structure differences from the other configurations. In the B configuration, the adsorbed Si dimer is positioned on top of a silicon dimer substrate row, and the dimer bond of the adsorbed Si dimer is aligned perpendicular to the dimer bonds of the underlying substrate dimer row. In the A configuration, the adsorbed silicon dimer is also positioned on top of a substrate dimer row, but the bond of the adsorbed dimer is aligned along the dimer bonds of the underlying substrate dimer row. At room temperature, the adsorbed dimer rotates back and forth between the orthogonal B and A states in less than 1 s. In the A configuration, the silicon dimer is slightly closer (approximately 0.15 Å) to the surface than in the B configuration (10). Therefore, the state of the dimer is reflected in the *z*-feedback position as a function of time. Clearly, at any given time the dimer has a higher probability of being found in state B, which is a consequence of its more favorable binding free energy. Also, the kinetics of the two states are quite different, as is reflected in the residence time (the amount of time that the dimer spends in a state before making a transition). The dimer has a much shorter residence time in state A than in state B. The ratio of these averaged residence times immediately gives the energy difference between both states,

$$\left(\frac{\langle\tau_B\rangle}{\langle\tau_A\rangle}\right) = e^{-(E_B-E_A)/k_B T},$$

provided that the attempt frequencies of both states are the same. If the latter condition is not satisfied, one should measure the temperature dependence of the residence times. The averaged residence times of both states give the kinetic barriers that separate both states, i.e.,

$$\langle\tau_{A,B}\rangle = \tau_0 e^{-E_{A,B}/k_B T},$$

where $\tau_0 = 1/\nu_0$ and where ν_0 is the attempt frequency. (ν_0 is typically on the order of 10^{12} – 10^{13} Hz.)

Note that the term TRSTM was first used for the combination of STM with (quantum) optical techniques (11–19). The high spatial resolution of the STM and the high temporal resolution offered by ultrashort laser pulses enable high-bandwidth measurements based on the pump-probe technique. The aim of this technique is to achieve simultaneously unprecedented spatial and temporal resolution. However, high spatial and temporal resolutions are difficult to establish simultaneously: The measurement bandwidth of the STM is typically limited by external electronics to ~50–500 kHz, and the spatial resolution of the laser technique is generally limited to its wavelength.

2.2. Open-Loop Spectroscopy

A few years after the closed-loop experiments by Swartzentruber et al. (9), Sato and coworkers (20) recorded similar time traces of the tunneling current in the open-loop configuration of a germanium dimer of the bare Ge(001) surface. The latter approach does not suffer from the low time resolution because the feedback loop is switched off. In this case, the time resolution is determined by the much larger bandwidth of the I - V converter, which has a typical bandwidth ranging from 50 to 600 kHz). Since the beginning of the twenty-first century, this technique has undergone rapid growth, and a large number of papers have appeared in high-impact journals (21–27).

In this section, we provide an example of a series of open-loop TRSTM experiments performed on a bare Ge(001) surface. To explain these experiments properly, we offer a brief description of semiconductor IV (001) surfaces. Silicon and germanium semiconductor group IV (001) surfaces are among the most frequently studied surfaces in the literature (28–30). Unreconstructed Si and Ge(001) surfaces have two broken bonds (i.e., dangling bonds) per surface atom. This high density of dangling bonds per surface atom is, from an energetic point of view, very unfavorable, as the free energy per unit area of a surface scales with the number of broken bonds per surface atom. However, the (001) surfaces reconstruct via the formation of surface dimers. This dimerization leads to a reduction in the number of dangling bonds from two per surface atom in the unreconstructed case to only one per surface atom in the reconstructed (i.e., dimerized) case. In addition to the short-range interaction that leads to dimerization, (001) surfaces also exhibit a weaker long-range interaction that leads to various higher-order surface reconstructions, such as $p(2 \times 2)$ and $c(4 \times 2)$. In 1985, the first STM images of the Si(001) surface (31, 32) revealed that most surface dimers have a symmetric appearance. However, as has been well established since the late 1970s, the lowest-energy configuration is a buckled dimer (33), and the observed symmetric dimers actually flip-flop rapidly between the two possible buckled configurations. The first direct evidence for this flip-flop motion was provided by Sato et al. (20), who demonstrated that the tunneling current recorded above one of the atoms of a dimer of the Ge(001) surface exhibited a telegraph-like noise. Subsequently, similar experiments were reported for Si(001) by Hata et al. (21), Yoshida et al. (22), and Pennec et al. (24). The latter measurements demonstrated that the flip-flop motion of the dimers can be interpreted as a so-called phason. A phason is a phase defect or antiphase boundary in the dimer alignment. At sufficiently high temperatures, these phasons perform a thermally activated (biased) random walk. If at an antiphase boundary one of the dimers flips to its other buckled configuration, the phason effectively moves by one lattice spacing. A dimer that is positioned under an STM tip thus flips to its other buckled configuration each time a phason traverses the tunnel junction. Such an event leads to a jump in the tunneling resistance and thus to a jump in the tunneling current.

Figure 1a shows a room-temperature STM image of the Ge(001) surface. The surface shows an ordered $c(4 \times 2)/(2 \times 1)$ domain pattern. Within a single substrate dimer row, the dimers nearly always buckle in an antiferromagnetic order, meaning that neighboring dimers buckle in opposite directions. The antiferromagnetic order partially relaxes the stress generated by the buckling of the dimers. In-phase buckling of adjacent dimer rows leads to a $p(2 \times 2)$ reconstruction, whereas out-of-phase buckling of adjacent dimer rows leads to a $c(4 \times 2)$ reconstruction. In the two latter cases, the asymmetric appearance of the dimers is generally perceived to imply that the flip-flop motion is frozen in.

We have performed room temperature measurements of the flip-flop motion of dimers ordered in (2×1) and $c(4 \times 2)$ domains (**Figure 1b**). Interestingly, the flickering indicated in the figure is not only observed in the dimer row that appears symmetric, but also in the row that appears

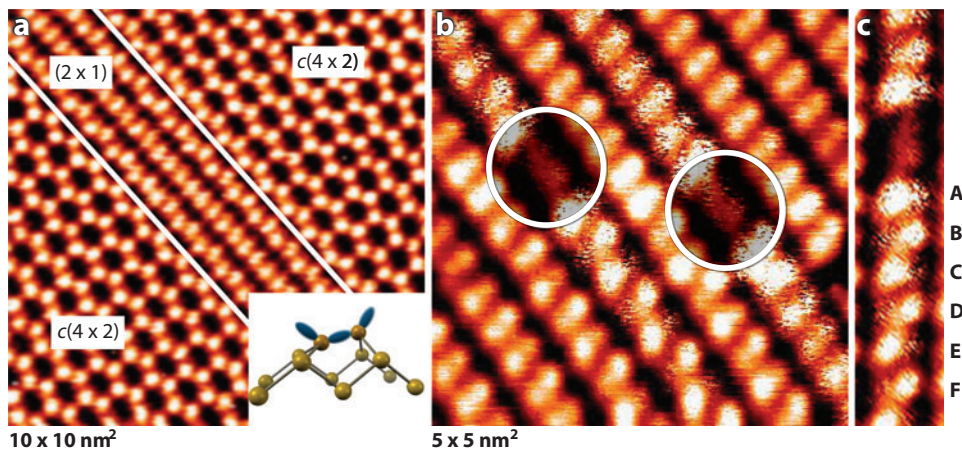


Figure 1

(a) Filled-state room temperature scanning tunneling microscopy (STM) image of Ge(001). The sample bias (V_{bias}) is -1.5 V, and the tunneling current (I_{tunnel}) is 0.4 nA. The local $c(4 \times 2)$ and (2×1) reconstructions are indicated. The phase boundary between the two domains is indicated by white lines. (Inset) Schematic representation of a buckled dimer. The tilt angle of the dimer bond is approximately 10° – 20° . (b) Filled-state STM image of Ge(001) ($V_{\text{bias}} = -1.5$ V, $I_{\text{tunnel}} = 0.4$ nA). The flickering in some of the substrate dimer rows is due to the flip-flop motion of the dimers during imaging. The flickering is most pronounced in dimer rows that contain missing dimer defects. Note that this flickering occurs in a symmetric dimer row (right defect) as well as in an asymmetric dimer row (left defect). (c) The dimer positions where the current is measured as a function of time are labeled A through F. Data taken from Reference 25.

asymmetric. This observation conflicts directly with the picture of static buckled dimers in the $c(4 \times 2)$ phase. Importantly, there are also buckled dimers that exhibit no flip-flop motion, at least not on the timescale that is accessible to our instrument. Their motion is either too slow or too fast for us to observe.

The flip-flop motion of the dimers is a consequence of phase defects in the dimer alignment. The dimer under the tip is flipped each time a phason makes an in-plane traversal of the tip-surface junction. To investigate the dynamics of the dimer flip-flop motion in more detail, the tunneling current is measured as a function of time at various dimer sites (Figure 1c). To correct for the attractive interaction between the tip and the diffusing phasons, as described by Pennec et al. (24), the tunneling current is measured over each pixel of the STM picture. Figure 2a shows a typical current trace. The telegraph noise indicates that the asymmetric dimer has a preference for one of the buckled states, whereas the flickering symmetric dimer exhibits no such preference. The flip-flop frequency of the nonflickering symmetric dimer is probably so high that it lies outside the bandwidth of the preamplifier (~ 50 kHz). The distribution of the residence times of the dimers in each of the two buckled states is shown in a histogram for the symmetric dimers in Figure 2b and for the asymmetric dimers in Figure 2c–f. Assuming that the flip-flop motion is a random process, the theoretical lines are obtained from the relation

$$H(t) = \frac{N}{2} p_{ij} (1 - p_{ij})^t, \quad (1)$$

where p_{ij} is the probability of flipping from state i to state j , N is the number of flip-flop events, and t is the time. The factor $N/2$ results from the fact that half of the flip-flop events are from state i to state j and the other half are from state j to state i . N and p_{ij} are determined from the distribution of the residence times. The average residence times of the two configurations of the symmetric dimer

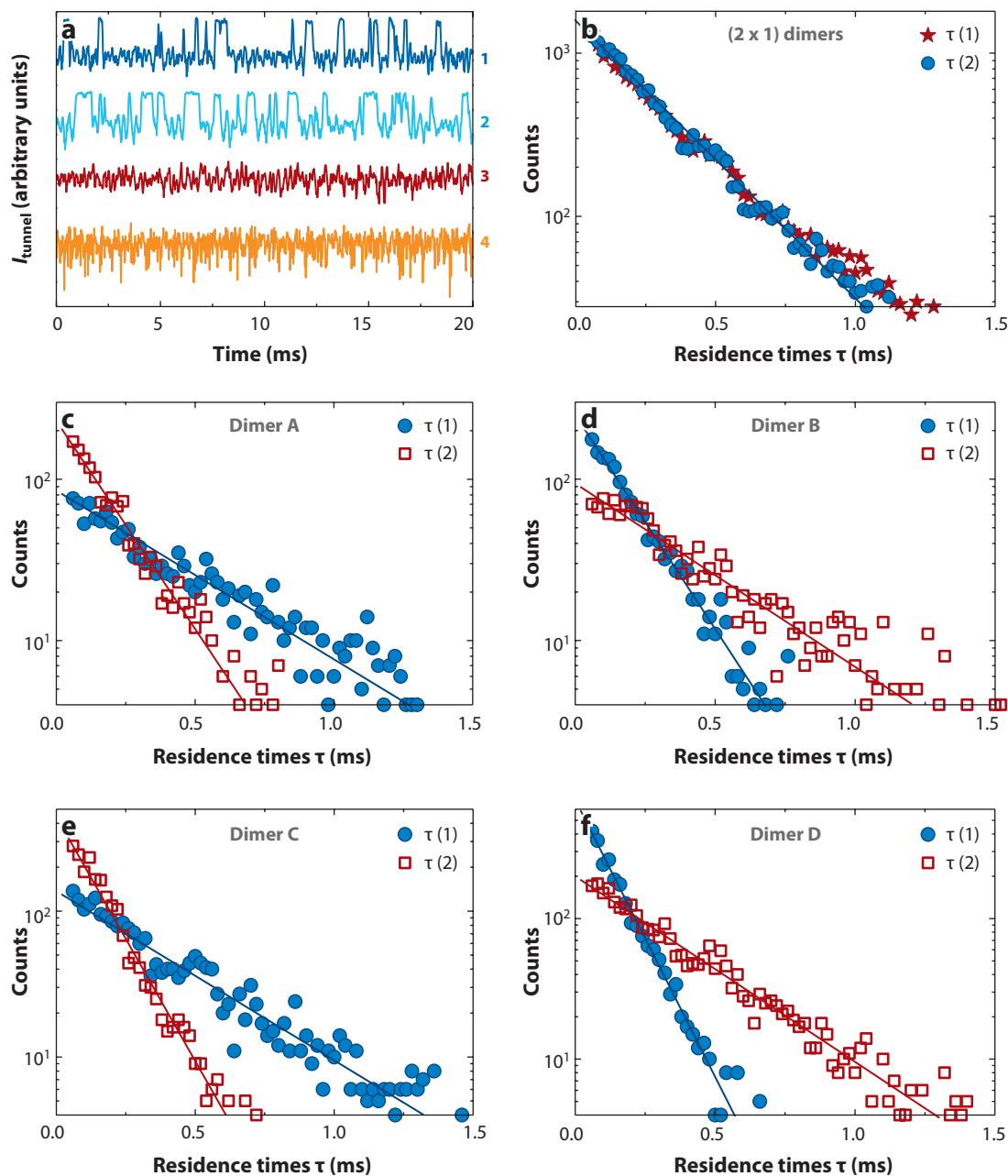


Figure 2

(a) Current traces measured on a flickering asymmetric dimer (curve 1), a flickering symmetric dimer (curve 2), a nonflickering symmetric dimer (curve 3), and a nonflickering asymmetric dimer (curve 4). The sampling rate is 50 kHz. (b) Histogram of the residence times in the two buckled states of a symmetric-appearing dimer. The line is the theoretical fit for a random process (Poisson distribution). $\tau(1)$ and $\tau(2)$ are the counts for the two residence times in the two different states. (c–f) Histograms of the residence times for dimers A–D. The lines are the corresponding theoretical curves for a random process. As in panel b, $\tau(1)$ and $\tau(2)$ are the counts for the two residence times in the two different states. Data taken from Reference 25.

are approximately the same, whereas they are significantly different for the asymmetric-appearing dimers labeled A–D (**Figure 2**). The distribution of residence times in states i and j (for dimer A state i is more favorable, for dimer B state j , for dimer C state i , etc.) is in accordance with the observed $\alpha(4 \times 2)$ reconstruction in this row. The difference in average residence times of the asymmetric-appearing dimers allows us to determine the energy difference of the two buckled configurations. It is obvious that this simple, but elegant, open-loop TRSTM technique allows us to study a large variety of dynamical processes, including conformational changes, rotation, and diffusion of single molecules.

3. SCANNING TUNNELING SPECTROSCOPY

3.1. Current–Voltage Spectroscopy

In this section we elaborate upon the best-known spectroscopic mode of STM, namely scanning tunneling spectroscopy (STS). First, however, we briefly describe a theory that was put forward in the early years of STM. The first detailed theoretical description of the tunneling process in STM was launched by Tersoff & Hamann (34, 35) in the mid-1980s. In the Tersoff-Hamann model, the wave functions of the substrate and the tip are considered as separated, undisturbed systems. Using time-dependent perturbation theory, Tersoff and Hamann calculated the wave function of the total system. In their approach, the potential of the tip is described as a perturbation, $V_{tip}(t)$, and is plugged into the time-dependent Schrödinger equation

$$\hbar \frac{\partial \psi_n}{\partial t} = \left[-\frac{\hbar^2}{2m} \frac{\partial^2}{\partial x^2} + V_{sub} + V_{tip}(t) \right] \psi_n, \quad (2)$$

where V_{sub} refers to the potential of the substrate and ψ_n refers to the wave function of the n th state. The wave function $\psi_n(x, t)$ is often assumed to have the form $\psi_n(x, t) = \psi(x)e^{-iE_n t/\hbar}$. The transition probability w_{nm} of an electron tunneling from the n th state into the m th state can be written as

$$w_{nm} = \frac{2\pi}{\hbar} |M_{nm}|^2 \delta(E_m - E_n), \quad (3)$$

where M_{nm} corresponds to the matrix element of the transition probability. This matrix element can be written in terms of a surface integral (36),

$$M_{nm} = -\frac{\hbar^2}{2m} \int (\psi_m^* \nabla \psi_n - \psi_m \nabla \psi_n^*) dS, \quad (4)$$

where dS is a surface element. The tunneling current is calculated by summing up over all possible electronic states. If the density of states (DOS) of the tip and the substrate are represented by ρ_{tip} and ρ_{sub} , respectively, one obtains

$$I = \frac{4\pi e^2}{\hbar} V \rho_{sub}(E_F) \rho_{tip}(E_F) |M|^2, \quad (5)$$

where V is the sample bias and E_F is the Fermi level. Assuming that only s -like wave functions contribute to the tunneling from the tip with radius R , the DOS of the tip near the Fermi level can be represented by

$$\rho_{tip}(E_F) \propto |\psi_n|^2 \propto e^{-2\kappa(R+z)}, \quad (6)$$

where z is the distance from tip to substrate and κ is the inverse decay length given by

$$\kappa = \sqrt{\frac{2m(\phi_{tip} + \phi_{sub})}{\hbar^2} - E + \frac{eV}{2}}. \quad (7)$$

Here $\phi_{tip,sub}$ is the work function of the tip (substrate), and E is the energy of the state relative to the Fermi level. In Equation 7 we assume that only electron states near the Γ point of the surface Brillouin zone contribute to the tunneling. If the latter condition is not satisfied, Equation 7 should be replaced by

$$\kappa = \sqrt{\frac{2m(\phi_{tip} + \phi_{sub})}{\hbar^2} - E + \frac{eV}{2} + k_{\parallel}^2}, \quad (8)$$

where k_{\parallel} is the parallel momentum of the surface electronic state.

Because the STM tip is usually a metal, the DOS of the tip can be assumed to be featureless. For illustrative purposes, we can write an approximate expression for the tunneling current as

$$I \propto \int_0^{eV} \rho_{sub}(E) T(E, eV) dE, \quad (9)$$

where $T(E, eV) = e^{-2\kappa z}$ is the transmission probability of the electron. The derivative, dI/dV , is given by

$$dI/dV \propto e \rho_{sub}(eV) T(eV, eV) + e \int_0^{eV} \rho_{sub}(E) \frac{d}{d(eV)} (T(E, eV)) dE. \quad (10)$$

Although Equation 10 is useful for determining, for instance, the band gap of a semiconductor, it only gives an idea of the LDOS at the Γ point of the surface Brillouin zone. Nevertheless, one can numerically extract the LDOS through the normalization process of $(dI/dV)/(I/V)$ (i.e., $d \ln I / d \ln V$) (37–39):

$$\frac{dI/dV}{I/V} = \frac{\rho_{sub}(eV) + \int_0^{eV} \frac{\rho_{sub}(E)}{T(eV, eV)} \frac{d}{d(eV)} (T(E, eV)) dE}{\frac{1}{eV} \int_0^{eV} \rho_{sub}(E) \frac{T(E, eV)}{T(eV, eV)} dE}. \quad (11)$$

Because $T(E, eV)$ and $T(eV, eV)$ appear as ratios in the numerator and denominator of this equation, their exponential dependences on V and z tend to cancel (38). The first term in the numerator of Equation 11 is simply the LDOS of the substrate. For $V > 0$ (the empty states of the sample are probed), $T(E, eV) \leq T(eV, eV)$, and the maximum transmission occurs at $E = eV$. Because all the terms in Equation 11 are of the same order of magnitude, we find a normalized measure of the DOS in conjunction with a slowly varying background. For $V < 0$ (the filled states of the sample are probed), $T(E, eV) \geq T(eV, eV)$, and the maximum transmission now occurs at $E = 0$. The background term and the term in the denominator are of the same order, but both are larger than the DOS term. Therefore, it is usually more difficult to probe the low-lying filled surface states of the substrate. **Figure 3** shows an example of the LDOS (dI/dV) recorded on the (2×1) and $c(4 \times 2)$ domains of a Ge(001) surface at room temperature (40).

3.2. dI/dV Mapping

In the preceding subsection, LDOS curves were obtained by collecting I - V traces over a relatively large surface area. If we assume a well-ordered surface with a spatially varying electronic structure, we can attempt to make a spatial map of the various electronic states (41–45). To illustrate a surface with a well-ordered electronic structure, we use a Pt-modified Ge(001) surface. If a monolayer or submonolayer amount of Pt is deposited on a Ge(001) surface and is subsequently annealed to temperatures above 1050–1100 K, well-ordered arrays of Pt chains develop (46, 47). The Pt chains have a cross section of only one atom, are kinkless, and are virtually defect free. **Figure 4a** presents an STM image of such a surface. The nearest-neighbor spacing between the Pt chains is 1.6 nm, although, occasionally, Pt nanowires spaced 2.4 nm apart may also occur. The latter spacing is found when two Pt nanowire patches are out of phase with one another.

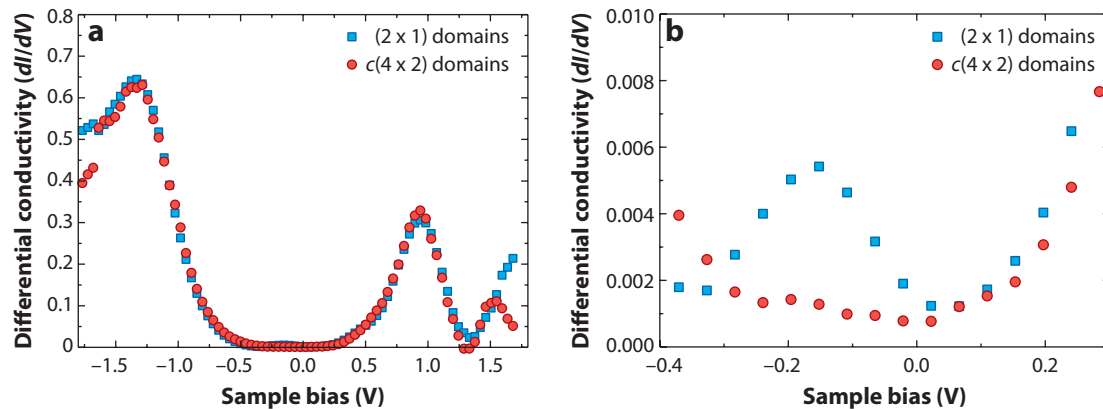


Figure 3

(a) The differential conductivity as recorded on the (2×1) and $c(4 \times 2)$ domains of a Ge(001) surface. The data are taken at room temperature. The peaks at -1 V and 0.8 V can be assigned to the dimer bond and to its antibonding partner, respectively. The small peak just below the Fermi level (b) is the only clear difference between the two domains. The metallic peak of the (2×1) domains is assigned to the continuous charge transfer between the dangling π bonds during the flip-flop motion. The static symmetric dimer configuration is believed to be metallic, as the dangling bonds of atoms of the dimer contain precisely one electron per bond. Data taken from Reference 40.

Shown in **Figure 5a** are the spatially averaged LDOS [i.e., the normalized derivative $(dI/dV)/(I/V)$] between Pt nanowires spaced 1.6 nm and 2.4 nm apart. The corresponding spatial map is shown in **Figure 4b**. Because the measurements in **Figure 4a,b** were recorded simultaneously, the images can be superimposed (**Figure 4c**). The data clearly show that the electronic state is exclusively present in the troughs between the Pt nanowires.

In the $(dI/dV)/(I/V)$ curve of the Pt nanowires with an interwire distance of 2.4 nm, two peaks are observed at 40 and 160 meV above the Fermi level. The energy positions of these one-dimensional electronic states are in perfect agreement with the energy levels of a quantum particle in a well of width L , i.e., $E = \frac{\hbar^2 \pi^2}{2mL^2} n^2$ (**Figure 5b**). For $L = 1.6$ nm, only the first state ($n = 1$) can be observed, whereas for $L = 2.4$ nm, the $n = 1$ as well as the $n = 2$ states can be observed.

For a one-dimensional system, the DOS is expected to behave as $\text{DOS}(E) \propto (E - E_n)^{-1/2}$, where E_n is the energy position of the n th state (the van Hove singularity). In the measured LDOS (**Figure 5a**), however, these peaks are more broad. There are two reasons for the broadening of these peaks: (a) a thermal broadening and (b) an experimental broadening because the dI/dV data are recorded with a modulation voltage of 10 mV. Both effects result in a total broadening of ~ 35 meV, which agrees well with the observed shape of both peaks (48). Most noticeable is the relatively large contribution ($\sim 40\%$) of the tail of the $n = 1$ state to the total DOS at the onset of the $n = 2$ peak (i.e., at E_2).

The lateral distribution of the LDOS is proportional to $|\Psi_n(x)|^2$. Therefore, one expects a lateral distribution that behaves as $\sin^2(\frac{n\pi x}{L})$, i.e., a maximum at $x = \frac{L}{2}$ for the $n = 1$ state and a minimum at $x = \frac{L}{2}$ for the $n = 2$ state. The cross section of the spatial map of the $n = 1$ state agrees well with the expected distribution (**Figure 5c**). At first sight, the measured distribution of the $n = 2$ state seems to disagree with the expectations (see **Figure 5d**). However, at 160 meV both $n = 1$ and $n = 2$ states contribute, as shown in **Figure 5a**. In order to resolve the spatial variation of the $n = 2$ state, the contribution of the tail of the $n = 1$ state at 160 meV should be subtracted.

The corrected spatial variation of the $n = 2$ state (**Figure 5d**) now resembles the expected lateral distribution of $|\Psi_2(x)|^2$, with a nice minimum in the middle of the trough. In addition, spatial

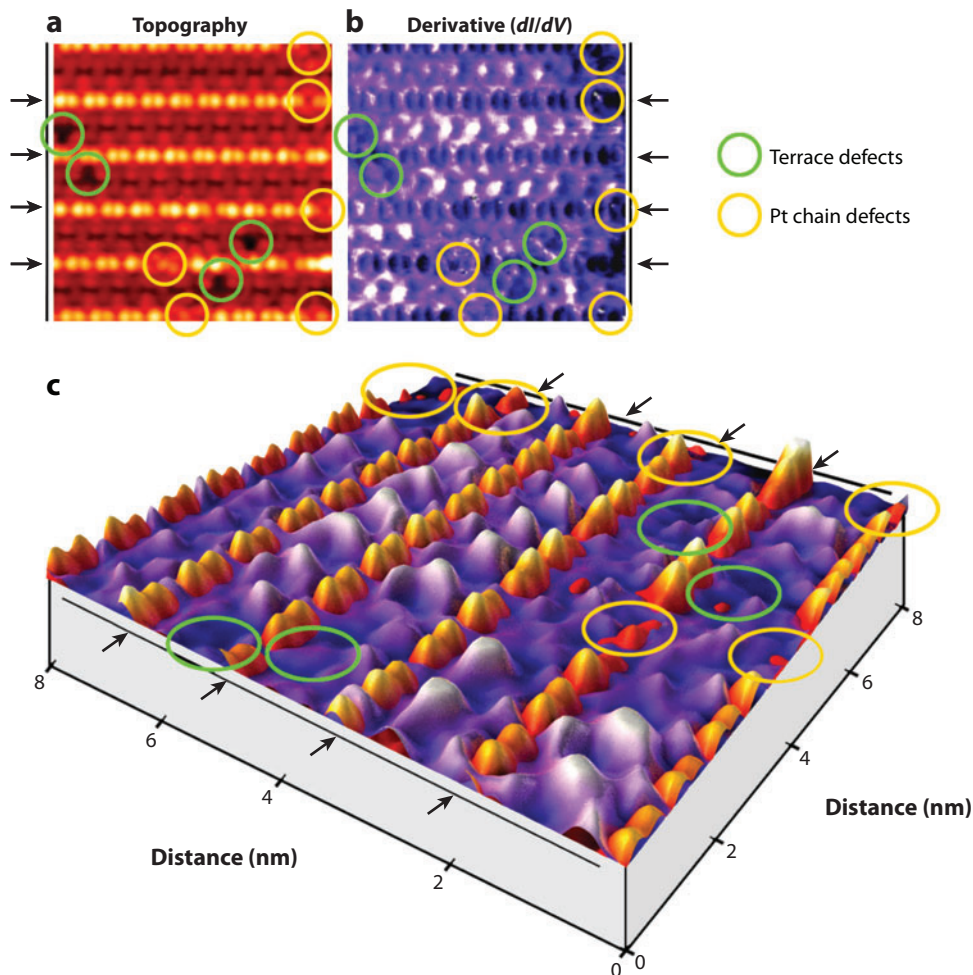


Figure 4

Topography (*a*) and spatial map of the differential conductivity (dI/dV) (*b*) of an $8\text{ nm} \times 8\text{ nm}$ area with several Pt nanowires recorded at 77 K. The sample bias is 0.15 V, and the tunnel current is 0.437 nA. (*c*) A three-dimensional representation of the topography (yellow/red) and dI/dV map (purple) is shown. The one-dimensional electronic state is exclusively located in the troughs of the Pt nanowires (indicated by arrows). The ellipses represent defects in the Pt nanowire and in the underlying substrate, respectively. The confinement of the electronic state vanishes near the defects. Data taken from Reference 47.

mapping at energies ranging from 170 to 250 meV clearly show that, with increasing energy, the dip in the LDOS distribution at $x = \frac{L}{2}$ increases. This is because the influence of the $n = 1$ tail decreases with increasing energy (sample bias).

3.3. Single-Electron Tunneling Phenomena

In principle, the quantization of the electron charge can be measured by probing the electron transport through a small metallic cluster coupled via two tunnel junctions to an external circuit. To detect the discreteness of the electron in such a circuit, two requirements must be met: (*a*) the

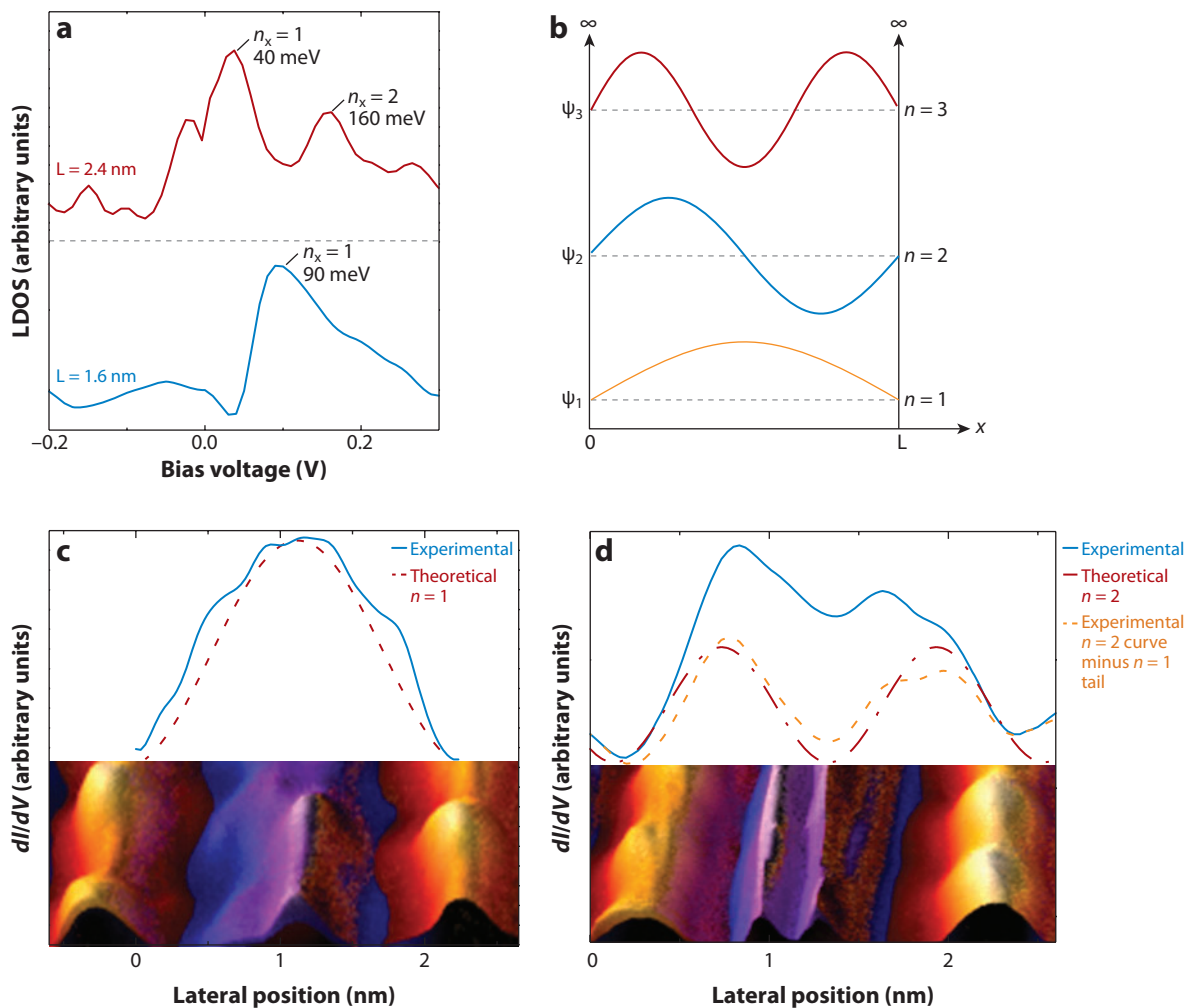


Figure 5

(a) Normalized derivative (dI/dV) recorded as a function of the sample bias for Pt nanowires with a nearest-neighbor spacing of 1.6 nm (bottom curve) and 2.4 nm (top curve), respectively. The data were taken at 77 K. (b) Schematic diagram of the $n = 1, 2$, and 3 states of a quantum mechanical particle in a box. (c) Spatially averaged cross section of the differential conductivity between nanowires with separation of 2.4 nm recorded at 40 mV. The solid line represents experimental data, and the dotted line indicates the $n = 1$ state of a quantum mechanical particle in a box. (d) Spatially averaged cross section of the differential conductivity between nanowires with separation of 2.4 nm recorded at 160 mV. The blue solid line represents experimental data, and the red dotted line indicates the $n = 2$ state of quantum mechanical particles in a box. The orange dotted line indicates the experimental data corrected for the contribution of the tail of the $n = 1$ state. Abbreviation: LDOS, local density of states. Data taken from Reference 48.

total capacitance of the cluster to its environment should be so small that the charging energy $e^2/2C$ is larger than the thermal energy $k_B T$ and (b) the resistances of both tunnel junctions must be larger than the quantum resistance, $h/2e^2$ (49–52). STS is a simple and elegant technique for measuring these SET phenomena on nanoscale junctions (53). The simplest configuration consists of an STM tip that acts as an electrode, a small metal cluster (usually Au or Ag), and an ultrathin oxide layer formed on top of a conductive substrate, which acts as the second electrode. It is also possible to use a colloidal particle coated with a thin insulating shell as the key element of

SAM: self-assembled monolayer

a double-junction system (54). Organic molecules can also be used to produce stable and reliable tunneling barriers.

In addition, self-assembled monolayers (SAMs) of organic molecules on metal substrates are a popular starting point for nanoscale circuit device applications. There are several advantages of using SAMs. First, they are easy to prepare, and they form highly ordered and very stable layers on metal surfaces such as Au, Ag, and Pt. Moreover, the possibility to use molecules with different lengths allows one to precisely control the resistance and thickness of the monolayer. Here we discuss a SAM made of decanethiol ($\text{CH}_3(\text{CH}_2)_9\text{SH}$) molecules. The most important reason for choosing this molecule is its high resistance. Previous experiments and detailed theoretical studies have revealed that the resistance of an alkanethiol molecule depends exponentially on the length of the molecule, as expected from coherent and nonresonant tunneling (55–57). In this instance, the double junction is realized by depositing small Pd clusters, generated by pulsed laser deposition, on top of the SAM (58, 59). The STM image shown in **Figure 6** reveals that the Pd clusters, which typically measure only a few nanometers in diameter, are randomly deposited onto the SAM. In order to determine whether the Pd clusters are electrically insulated from the surface, one can record I - V traces on the clusters and compare them with I - V traces recorded on the bare SAM.

In this experiment, I - V spectra were recorded at each point of the STM image. The difference between the appearances of the curves shown in **Figure 6a,b** (staircase-like versus linear) suggests that the measured staircase is due to a Coulomb charging effect of the Pd clusters located on top of the decanethiol monolayer. A closer look at the data reveals that the staircase-like curve (**Figure 6a**) is slightly asymmetric. This asymmetry may be due to a small fractional charge that is a direct consequence of a polarization of charge arising from the asymmetry of the two electrodes.

To make model calculations for the staircase-like curve, the orthodox theory of SET can be applied (50, 60–61). By using a simple fitting algorithm, the absolute minimum in the mean square deviation of the experimental I - V curve from the theoretical I - V curve can be determined. There are four parameters to fit: C_1 , C_2 , R_1 , and R_2 (i.e., the capacitances and resistances of both tunnel junctions). Note that even at room temperature, Coulomb blockade oscillations can be measured. This is only possible if the total capacitance $C = C_1 + C_2$ is smaller than $e^2/k_B T$, i.e., 5×10^{-18} F.

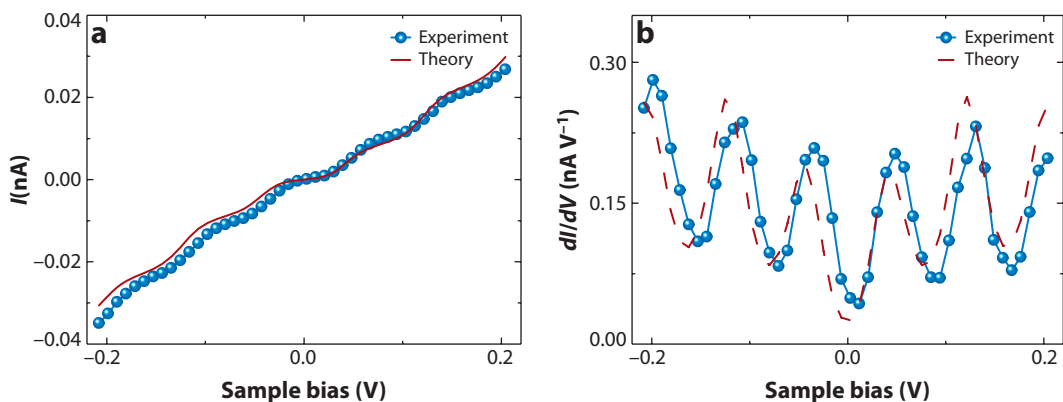


Figure 6

(a) Experimental (blue circles) and theoretical (red line) current–voltage (I - V) curve recorded at 77 K on a small Pd cluster deposited on a decanethiol self-assembled monolayer (SAM). The curve clearly demonstrates staircase-like behavior. (b) dI/dV versus voltage. Each oscillation corresponds to the addition or subtraction of one electron. The curve was recorded on top of the bare SAM and exhibits simple linear behavior. Data taken from Reference 58.

4. I - z SPECTROSCOPY

4.1. Work Function

In Section 3.1. we showed that the tunneling current depends exponentially on the tip-surface separation, i.e., $I \propto e^{-2\kappa z}$. In **Figure 7**, we present a plot of current versus distance as recorded on a Pt-modified Ge(001) sample. As shown in Equation 7, the inverse decay length, κ , provides information on the average or effective work function of tip and substrate, $\bar{\phi} = (\phi_t + \phi_s)/2$. For large tip-surface separations, the effective work function must approach the surface local work function, which is defined as the work needed to remove an electron from the solid's Fermi level to a position far away from the surface so that image force effects can be neglected. For tip-surface separations measuring up to approximately 1 nm, image potential effects cannot be ignored. As a first-order approach, one can replace the effective work function by $\bar{\phi}_0 - \frac{\alpha}{d}$, where $\bar{\phi}_0$ is the real average work function of the substrate and the tip; d is the distance between two image planes, which deviates from the distance between the two metal electrodes; and α is a constant of approximately 10 eV \AA^{-1} .

The work function of the substrate may exhibit some spatial variation, which can easily be determined because the work function of the tip is fixed. The most straightforward way to determine the effective work function $\bar{\phi}$ is to open the feedback loop and quickly measure the current I as a function of the tip-surface separation z (62–64). Subsequently, $\ln(I)$ can be plotted versus the tip-surface separation:

$$\ln(I) \approx -2 \left(\sqrt{\frac{2m\bar{\phi}}{\hbar^2} - E + \frac{eV}{2}} \right) z. \quad (12)$$

If the sample bias is small, and if we ignore the electronic structure of the substrate and the tip, the effective work function can be extracted from the slope of the $\ln(I)$ versus the z curve.

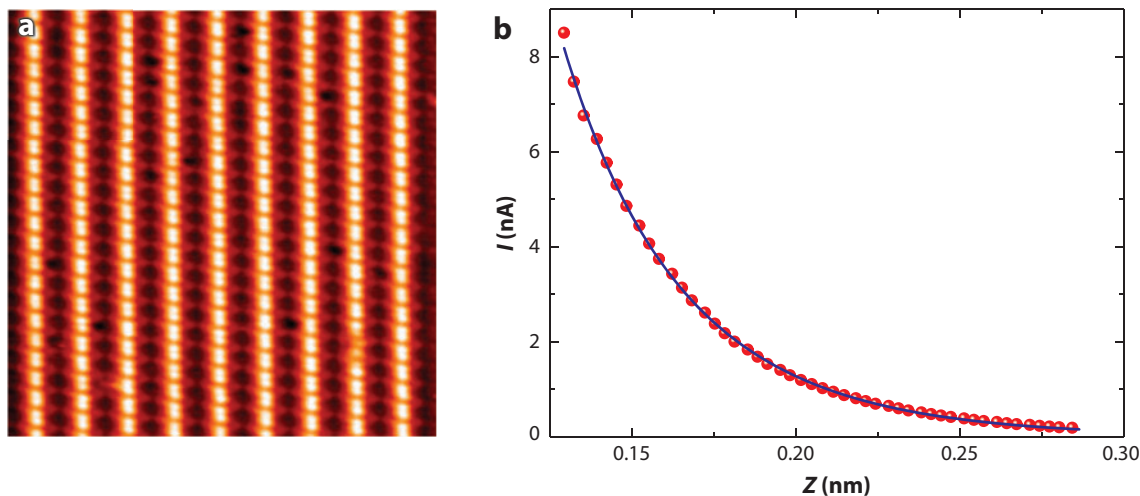


Figure 7

(a) Filled-state image of a Pt-modified Ge(001) surface recorded at 77 K. The sample bias is -1.0 V , the tunnel current is 0.4 nA , and the image size is $15 \text{ nm} \times 15 \text{ nm}$. (b) Spatially averaged current versus distance (I - z) curve (circles) recorded on a Pt-modified Ge(001) at 77 K. The solid line is a fit based on the Simmons model. Data taken from Reference 64.

4.2. Gundlach Oscillations

The STM can also be operated in the field-emission regime and in the Fowler-Nordheim regime, in which the applied bias voltage exceeds the averaged work function of substrate and tip (the typical work function for metals is approximately 4–5 eV). Under this condition, the electrons at the Fermi level that dominantly contribute to the tunneling current are partly reflected at the surface, then reflected again at the rising potential within the tunneling barrier. Thus, electron standing waves can be excited in the vacuum gap in front of the substrate surface. The condition for the development of this standing wave pattern depends on the exact shape of the electronic potential in the vacuum gap, the reflection coefficient at the surface, and the energy of the field-emitted electrons. The electron standing waves that may appear in a distance/voltage curve are known as Gundlach oscillations. Gundlach (65) calculated the tunneling current/transmission coefficient as a function of the applied bias voltage for a metal/insulator/metal system.

Coombs & Gimzewski (66) present an approximate description of the experimentally observed higher-order resonance states. The resonance condition is fulfilled if an integer number of half-wavelengths of the electron wave function fit into the well between sample and rising vacuum gap potential. Coombs and Gimzewski derived the condition

$$V_n = \phi + c(nF)^{2/3}, \quad (13)$$

where $c = (\frac{3\pi\hbar}{2\sqrt{2m}})^{2/3} \approx 4.39 \text{ V}^{1/3} \text{ \AA}^{2/3}$, V_n is the voltage of the n th resonance state, ϕ is the work function, and F is the field strength in volts per angstrom. Note that image forces are neglected here. These image forces mainly affect oscillations with small n values. In addition, we consider a quasi-one-dimensional electrical field distribution, whereas in reality the distribution is essentially three-dimensional.

The Gundlach oscillations can also be observed in standard I - V measurements, provided that the feedback loop is switched on. Closed-loop I - V spectra can be recorded by means of a lock-in technique (67, 68). In this mode, a small high-frequency oscillation is added to the bias, and the corresponding modulation of the tunneling current is measured.

5. INELASTIC ELECTRON TUNNELING SPECTROSCOPY

In 1985 Binnig et al. (69) developed a method to extract the vibrational structure of a single molecule. In their method, they relied on the IETS technique, which was developed by Jacklevic & Lambe (70) in the mid-1960s. Jacklevic and Lambe found that tunneling electrons can excite vibrational modes of a thin layer of molecules encapsulated in an oxide layer that was trapped between two metal electrodes. The oxide layer is so thin that it acts as a tunnel barrier for the electronic transport from one electrode to the other. The excitation of vibrations is a consequence of inelastic scattering processes that can take place during the tunneling process. If the electrons have sufficient energy to excite a vibrational mode, an additional channel for transport opens. Usually this leads to a small but abrupt increase in the tunnel current exactly at the onset of the threshold value for excitation. The resolution of these inelastic tunneling effects depends on two fundamental processes, namely excitation and detection. The excitation process allows conversion from the high-energy initial state to the excited state. This excited state is lower in energy than the initial state by an amount that equals the threshold value for excitation. The fraction of electrons that tunnel inelastically is related to the nature and alignment of electronic resonances associated with the molecule/surface systems and is usually less than 1% of the total current. At the threshold voltage for excitation, i.e., $\pm\hbar\omega/e$, a kink in the I - V curve is observed. Such a kink leads to a step in the dI/dV curve and to a peak in the d^2I/dV^2 curve. An important signature of an inelastic process is that it leads to two peaks, one peak at $+V$ and another inverted peak at $-V$.

A lock-in technique is usually used to detect peaks in the d^2I/dV^2 curve. This technique is implemented by adding a small alternating current high-frequency modulation to the sample bias and subsequently monitoring the tunnel current. The magnitude of the response oscillating with the double frequency yields a value proportional to d^2I/dV^2 . These signals are normally very small; therefore, they must be measured sufficiently slowly. Thus, the STM junction should be very stable, as the measurements are taken in the open-feedback-loop configuration. The required high stability of the STM junction is generally only achieved at very low temperatures. However, there is another reason why IETS measurements are preferably performed at low temperatures: the rather small thermal broadening of the d^2I/dV^2 peaks. The thermal broadening at approximately $5.4 k_B T$ results in a thermal broadening of ~ 2 meV at 4.2 K. The latter is already significantly larger than the intrinsic peak width W_i , which is less than 1 meV. Also, there is an additional instrumental broadening due to the fact that the d^2I/dV^2 spectra are recorded with a lock-in amplifier with amplitude V_{mod} . The total broadening, W , is given by

$$W = \sqrt{W_i^2 + (1.7V_{\text{mod}})^2 + \left(5.4 \frac{k_B T}{e}\right)^2}. \quad (14)$$

Therefore, most IETS measurements are recorded in the temperature window between 4 K and 20 K (71–73). The pioneering work in IETS was performed by Wilson Ho's group (71, 72). Ho and coworkers were the first to show that the STM-IETS technique can provide a chemical fingerprint of an individual molecule adsorbed on a surface. For example, **Figure 8** shows d^2I/dV^2 spectra

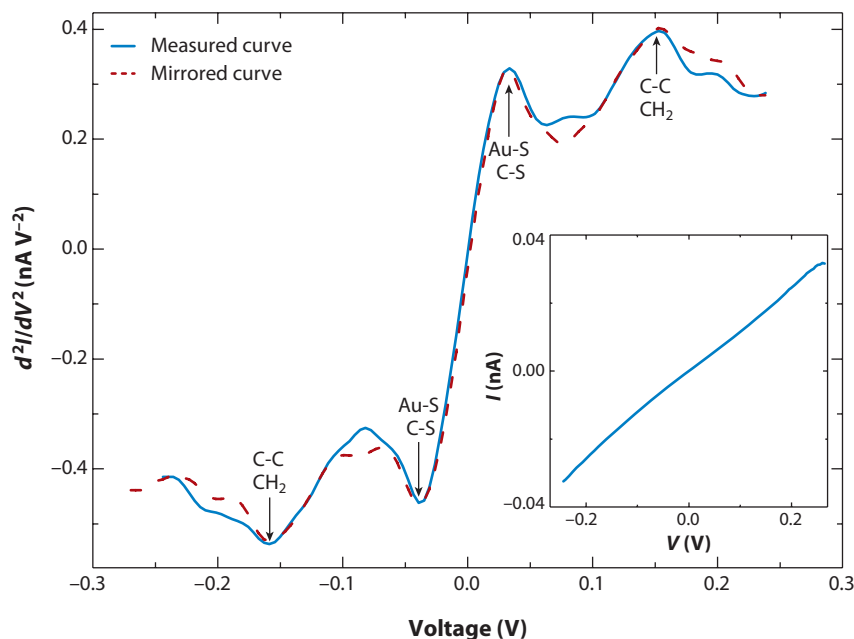


Figure 8

Inelastic electron tunneling spectrum of a decanethiol self-assembled monolayer at 77 K. The two peaks located at approximately ± 33 and ± 155 meV are well resolved. The first peak is due to the Au-S (29 meV) and/or the C-S stretch mode (38 meV); the second peak is probably induced by the C-C stretch mode (131 meV) and/or the CH₂ twist and wag modes (155 and 163 meV, respectively). Because decanethiol monolayers are destroyed at tunnel currents higher than ~ 50 pA, the maximum current was kept below 30 pA. (*Inset*) Current–voltage (I – V) curve recorded at the same time as the inelastic electron tunneling spectrum. Both curves are averages over 2500 curves. Data taken from Reference 74.

recorded at a decanethiol monolayer on a gold substrate at 77 K (74). The two peaks in the curve are well resolved.

6. CONCLUSIONS AND OUTLOOK

The STM, including all its spectroscopic modes, can be effectively used to probe solid-state and molecular materials at the spatial limit. This technique's versatility is reflected in a wide range of problems that have been successfully investigated, including (a) dynamical processes at surfaces, (b) electronic properties of surfaces and adsorbates, (c) SET phenomena, and (d) chemical identification on scales as small as that of a single molecule. These applications (and many others) have not only justified the importance of STM and STS in modern science and technology, but they will probably spur scientists to expand this technique even further.

DISCLOSURE STATEMENT

The authors are not aware of any affiliations, memberships, funding, or financial holdings that might be perceived as affecting the objectivity of this review.

ACKNOWLEDGMENTS

Our work is financially supported by the Stichting voor Fundamenteel Onderzoek der Materie (FOM, 03PR2208).

LITERATURE CITED

1. Knoll M, Ruska E. 1932. Das Elektronenmikroskop. *Z. Phys.* 78:318–39
2. Müller EW. 1951. The field ion microscope. *Z. Phys.* 131:136–42
3. Binnig G, Rohrer H. 1982. Scanning tunneling microscopy. *Helv. Phys. Acta* 55:726–35
4. Simmons JG. 1963. Generalized formula for the electric tunnel effect between similar electrodes separated by a thin insulating film. *J. Appl. Phys.* 34:1793–803
5. Simmons JG. 1963. Electric tunnel effect between dissimilar electrodes separated by a thin insulating film. *J. Appl. Phys.* 34:2581–90
6. Binnig G, Rohrer H. 1987. Scanning tunneling microscopy—from birth to adolescence. *Rev. Mod. Phys.* 59:615–25
7. Wiesendanger R. 1994. *Scanning Probe Microscopy and Spectroscopy*. Cambridge, UK: Cambridge Univ. Press
8. Stipe BC, Rezaei MA, Ho W. 1998. Single-molecule vibrational spectroscopy and microscopy. *Science* 280:1732–35
9. Swartzentruber BS, Smith AP, Jónsson H. 1996. Experimental and theoretical study of the rotation of Si Ad-dimers on the Si(001) surface. *Phys. Rev. Lett.* 77:2518–21
10. Zhang Z, Wu F, Zandvliet HJW, Poelsema B, Metiu H, Lagally MG. 1995. Energetics and dynamics of Si Ad-dimers on Si(001). *Phys. Rev. Lett.* 74:3644–47
11. Hamers RJ, Cahill DG. 1991. Ultrafast time resolution in scanned probe microscopies: surface photovoltage on Si(111)-(7 × 7). *J. Vac. Sci. Technol.* B9:514–18
12. Weiss S, Botkin D, Ogletree DF, Salmeron M, Chemia DS. 1995. The ultrafast response of a scanning tunnelling microscope. *Phys. Status Solidi B* 188:343–59
13. Groenveld RHM, van Kempen H. 1996. The capacitive origin of the picosecond electrical transients detected by a photoconductively gated scanning tunneling microscope. *Appl. Phys. Lett.* 69:2294–96
14. Freeman MR, Elezzabi AY, Steeves GM, Nunes G Jr. 1997. Ultrafast time resolution in scanning tunneling microscopy. *Surf. Sci.* 366:290–300
15. Feldstein MJ, Vohringer P, Wang W, Scherer NF. 1996. Femtosecond optical spectroscopy and scanning probe microscopy. *J. Phys. Chem.* 100:4739–48

16. Khusnatdinov NN, Nagle TJ, Nunes G Jr. 2000. Ultrafast scanning tunneling microscopy with 1 nm resolution. *Appl. Phys. Lett.* 77:4434–36
17. Gerstner V, Knoll A, Pfeiffer W, Thon A, Gerber G. 2000. Femtosecond laser assisted scanning tunneling microscopy. *J. Appl. Phys.* 88:4851–59
18. Takeuchi O, Morita R, Yamashita RM, Shigekawa H. 2002. Development of time-resolved scanning tunneling microscopy in femtosecond range. *Jpn. J. Appl. Phys.* 41:4994–97
19. Terada Y, Aoyama M, Kondo H, Taninaka A, Takeuchi O, Shigekawa H. 2007. Ultrafast photoinduced carrier dynamics in GaNAs probed using femtosecond time-resolved scanning tunnelling microscopy. *Nanotechnology* 18:044028
20. Sato T, Iwatsuki M, Tochihara H. 1999. Detection of the flip-flop motion of buckled dimers on a Ge(001) surface by STM. *J. Electron Microsc.* 48:1–7
21. Hata K, Sainoo Y, Shigekawa H. 2001. Atomically resolved local variation of the barrier height of the flip-flop motion of single buckled dimers of Si(100). *Phys. Rev. Lett.* 86:3084–87
22. Yoshida S, Kimura T, Takeuchi O, Hata K, Oigawa H, et al. 2004. Probe effect in scanning tunneling microscopy on Si(001) low-temperature phases. *Phys. Rev. B* 70:235411
23. Ronic F, Colonna S, Thorpe SD, Cricenti A, Le Lay G. 2005. Direct observation of Sn adatoms dynamical fluctuations at the Sn/Ge(111) surface. *Phys. Rev. Lett.* 95:156101
24. Pennec Y, Horn von Hoegen M, Zhu X, Fortin DC, Freeman MR. 2006. Dynamics of an Ising chain under local excitation: a scanning tunneling microscopy study of Si(100) dimer rows at 5 K. *Phys. Rev. Lett.* 96:026102
25. Van Houselt A, Van Gastel R, Poelsema B, Zandvliet HJW. 2006. Dynamics and energetics of Ge(001) dimers. *Phys. Rev. Lett.* 97:266104
26. Lastapis M, Martin M, Riedel D, Hellner L, Comtet G, Dujardin G. 2005. Picometer-scale electronic control of molecular dynamics inside a single molecule. *Science* 308:1000–3
27. Liljeroth P, Repp J, Meyer G. 2007. Current-induced hydrogen tautomerization and conductance switching of naphthalocyanine molecules. *Science* 317:1203–6
28. Dąbrowski J, Müssig HJ. 2000. *Silicon Surfaces and Formation of Interfaces*. River Edge, NJ: World Sci.
29. Zandvliet HJW. 2003. The Ge(001) surface. *Phys. Rep.* 388:1–40
30. Zandvliet HJW. 2000. Energetics of Si(001). *Rev. Mod. Phys.* 72:593–602
31. Tromp RM, Hamers RJ, Demuth JE. 1985. Si(001) dimer structure observed with scanning tunneling microscopy. *Phys. Rev. Lett.* 55:1303–6
32. Hamers RJ, Tromp RM, Demuth JE. 1986. Scanning tunneling microscopy of Si(001). *Phys. Rev. B* 34:5343–57
33. Chadi DJ. 1979. Atomic and electronic structures of reconstructed Si(001) surfaces. *Phys. Rev. Lett.* 43:43–47
34. Tersoff J, Hamann DR. 1983. Theory and application for the scanning tunneling microscope. *Phys. Rev. Lett.* 50:1998–2001
35. Tersoff J, Hamann DR. 1985. Theory of the scanning tunneling microscope. *Phys. Rev. B* 31:805–13
36. Bardeen J. 1961. Tunnelling from a many-particle point of view. *Phys. Rev. Lett.* 6:57–59
37. Kubby JA, Griffith JE, Becker RS, Vickers JS. 1987. Tunneling microscopy of Ge(001). *Phys. Rev. B* 36:6079–93
38. Feenstra RM, Stroscio JA, Fein AP. 1987. Tunneling spectroscopy of the Si(111)2 × 1 surface. *Surf. Sci.* 181:295–306
39. Hamers RJ, Avouris PH, Boszo F. 1987. Imaging of chemical-bond formation with the scanning tunnelling microscope-NH₃ dissociation on Si(001). *Phys. Rev. Lett.* 59:2071–74
40. Gurlu O, Zandvliet HJW, Poelsema B. 2004. Electronic properties of (2 × 1) and c(4 × 2) domains on Ge(001) studied by scanning tunneling spectroscopy. *Phys. Rev. Lett.* 93:066101
41. Crommie MF, Lutz CP, Eigler DM. 1993. Confinement of electrons to quantum corrals on a metal-surface. *Science* 262:218–20
- 41a. Crommie MF, Lutz CP, Eigler DM. 1993. Imaging standing waves in a 2-dimensional electron-gas. *Nature* 363:524–27
42. Bürgi L, Jeandupeux O, Hirstein A, Brune H, Kern K. 1998. Confinement of surface state electrons in Fabry-Perot resonators. *Phys. Rev. Lett.* 81:5370–73

43. Nilius N, Wallis TM, Ho W. 2002. Development of one-dimensional band structure in artificial gold chains. *Science* 297:1853–56
44. Wallis TM, Nilius N, Ho W. 2002. Electronic density oscillations in gold atomic chains assembled atom by atom. *Phys. Rev. Lett.* 89:236802
45. Meyer Chr, Klijn J, Morgenstern M, Wiesendanger R. 2003. Direct measurement of the local density of states of a disordered one-dimensional conductor. *Phys. Rev. Lett.* 91:076803
46. Gurlu O, Adam OAO, Zandvliet HJW, Poelsema B. 2003. Self-organized, one-dimensional Pt nanowires on Ge(001). *Appl. Phys. Lett.* 83:4610–12
47. Oncel N, van Houselt A, Huijben J, Hallböck AS, Gurlu O, et al. 2005. Quantum confinement between self-organized Pt nanowires on Ge(001). *Phys. Rev. Lett.* 95:116801
48. van Houselt A, Oncel N, Poelsema B, Zandvliet HJW. 2006. Spatial mapping of the electronic states of a one-dimensional system. *Nano Lett.* 6:1439–42
49. Likharev KK. 1988. Correlated discrete transfer of single electrons in ultrasmall tunnel-junctions. *IBM J. Res. Dev.* 32:144–58
50. Averin DV, Likharev KK. 1991. Single-electronics. In *Mesoscopic Phenomena in Solids*, ed. BL Altshuler, PA Lee, RA Webb, pp. 173–271. Amsterdam: Elsevier
51. Shekhter RI. 1973. Zero anomalies in the resistance of a tunnel junction containing metallic inclusions in oxide layer. *Sov. Phys. JETP* 36:747–50
52. Kulik IO, Shekhter RI. 1975. Kinetic phenomena and charge discreteness effects in granulated media. *Sov. Phys. JETP* 41:308–16
53. Schonberger C, van Houten H, Donkersloot HC. 1992. Single-electron tunneling observed at room-temperature by scanning tunneling microscopy. *Europhys. Lett.* 20:249–54
54. Schonberger C, van Houten H, Donkersloot HC, Van Der Putten AMT, Fokkink LG. 1992. Single-electron tunneling up to room-temperature. *Phys. Scr.* 45:289–91
55. Akkerman HB, Blom PWM, de Leeuw DM, de Boer B. 2006. Towards molecular electronics with large-area molecular junctions. *Nature* 440:69–72
56. Zhao J, Uosaki K. 2002. Formation of nanopatterns of a self-assembled monolayer (SAM) within a SAM of different molecules using a current sensing atomic force microscope. *Nano Lett.* 2:137–40
57. Wang W, Lee T, Reed MA. 2003. Mechanism of electron conduction in self-assembled alkanethiol monolayer devices. *Phys. Rev. B* 68:035416
58. Oncel N, Hallböck AS, Zandvliet HJW, Speets EA, Ravoo BJ, et al. 2005. Coulomb blockade of small Pd clusters. *J. Chem. Phys.* 123:044703
59. Speets EA, Dordi B, Ravoo BJ, Oncel N, Hallböck AS, et al. 2005. Noble metal nanoparticles deposited on self-assembled monolayers by pulsed laser deposition show Coulomb blockade at room temperature. *Small* 1:395–98
60. Hanna AE, Tinkham M. 1991. Variation of the Coulomb staircase in a 2-junction system by fractional electron charge. *Phys. Rev.* 44:5919–22
61. Ferry DK, Goodnick SM. 1997. *Transport in Nanostructures*. Cambridge, UK: Cambridge Univ. Press
62. Stroschio JA, Feenstra RM, Fein AP. 1987. Local state density and long-range screening of adsorbed oxygen-atoms on the GaAs(110) surface. *Phys. Rev. Lett.* 58:1668–71
63. Stroschio JA, Feenstra RM, Fein AP. 1986. Electronic-structure of the Si(111)2 × 1 surface by scanning-tunneling microscopy. *Phys. Rev. Lett.* 57:2579–82
64. de Vries RJ, Saedi A, Kockmann D, van Houselt A, Poelsema B, Zandvliet HJW. 2008. Spatial mapping of the inverse decay length using scanning tunneling microscopy. *Appl. Phys. Lett.* 92:174101
65. Gundlach KH. 1966. Zur Berechnung des Tunnelstroms durch eine trapezformige Potentialstufe. *Solid-State Electron.* 9:949–57
66. Coombs JH, Gimzewski JK. 1988. Fine-structure in field-emission resonances at surfaces. *J. Microsc.* 152:841–51
67. Kolesnychenko OY, Shklyarevskii OI, van Kempen H. 1999. Calibration of the distance between electrodes of mechanically controlled break junctions using field emission resonance. *Rev. Sci. Instrum.* 70:1442–46
68. Kolesnychenko OY, Kolesnichenko YA, Shklyarevskii OI, van Kempen. 2000. Field-emission resonance measurements with mechanically controlled break junctions. *Physica B* 291:246–55

69. Binnig G, Garcia N, Rohrer H. 1985. Conductivity sensitivity of inelastic scanning tunneling microscopy. *Phys. Rev. B* 32:1336–38
70. Jaklevic RC, Lambe J. 1966. Molecular vibration spectra by electron tunnelling. *Phys. Rev. Lett.* 17:1139
71. Stipe BC, Rezaei MA, Ho W. 1998. Single-molecule vibrational spectroscopy and microscopy. *Science* 280:1732–35
72. Ho W. 2002. Single-molecule chemistry. *J. Chem. Phys.* 117:11033–61; references therein
73. Sainoo Y, Kim Y, Komeda T, Kawai M. 2004. Inelastic tunneling spectroscopy using scanning tunneling microscopy on trans-2-butene molecule: spectroscopy and mapping of vibrational features. *J. Chem. Phys.* 120:7249–51
74. Hallbäck AS, Oncel N, Huskens J, Zandvliet HJW, Poelsema B. 2004. Inelastic electron tunneling spectroscopy on decanethiol at elevated temperatures. *Nano Lett.* 4:2393–95



Contents

A Conversation with John B. Fenn <i>John B. Fenn and M. Samy El-Shall</i>	1
Liquid-Phase and Evanescent-Wave Cavity Ring-Down Spectroscopy in Analytical Chemistry <i>L. van der Sneppen, F. Ariese, C. Gooijer, and W. Ubachs</i>	13
Scanning Tunneling Spectroscopy <i>Harold J. W. Zandvliet and Arie van Housetl</i>	37
Nanoparticle PEBBLE Sensors in Live Cells and In Vivo <i>Yong-Eun Koo Lee, Ron Smith, and Raoul Kopelman</i>	57
Micro- and Nanocantilever Devices and Systems for Biomolecule Detection <i>Kyo Seon Hwang, Sang-Myung Lee, Sang Kyung Kim, Jeong Hoon Lee, and Tae Song Kim</i>	77
Capillary Separation: Micellar Electrokinetic Chromatography <i>Shigeru Terabe</i>	99
Analytical Chemistry with Silica Sol-Gels: Traditional Routes to New Materials for Chemical Analysis <i>Alain Walcarius and Maryanne M. Collinson</i>	121
Ionic Liquids in Analytical Chemistry <i>Renee J. Soukup-Hein, Molly M. Warnke, and Daniel W. Armstrong</i>	145
Ultrahigh-Mass Mass Spectrometry of Single Biomolecules and Bioparticles <i>Huan-Cheng Chang</i>	169
Miniature Mass Spectrometers <i>Zheng Ouyang and R. Graham Cooks</i>	187
Analysis of Genes, Transcripts, and Proteins via DNA Ligation <i>Tim Conze, Alysha Shetye, Yuki Tanaka, Fijuan Gu, Chatarina Larsson, Jenny Göransson, Gbolamreza Tavoosidana, Ola Söderberg, Mats Nilsson, and Ulf Landegren</i>	215

Applications of Aptamers as Sensors <i>Eun Jeong Cho, Joo-Woon Lee, and Andrew D. Ellington</i>	241
Mass Spectrometry–Based Biomarker Discovery: Toward a Global Proteome Index of Individuality <i>Adam M. Hawkrigde and David C. Muddiman</i>	265
Nanoscale Control and Manipulation of Molecular Transport in Chemical Analysis <i>Paul W. Bohn</i>	279
Forensic Chemistry <i>Suzanne Bell</i>	297
Role of Analytical Chemistry in Defense Strategies Against Chemical and Biological Attack <i>Jiri Janata</i>	321
Chromatography in Industry <i>Peter Schoenmakers</i>	333
Electrogenerated Chemiluminescence <i>Robert J. Forster, Paolo Bertocello, and Tia E. Keyes</i>	359
Applications of Polymer Brushes in Protein Analysis and Purification <i>Parul Jain, Gregory L. Baker, and Merlin L. Bruening</i>	387
Analytical Chemistry of Nitric Oxide <i>Evan M. Hetrick and Mark H. Schoenfish</i>	409
Characterization of Nanomaterials by Physical Methods <i>C.N.R. Rao and Kanishka Biswas</i>	435
Detecting Chemical Hazards with Temperature-Programmed Microsensors: Overcoming Complex Analytical Problems with Multidimensional Databases <i>Douglas C. Meier, Baranidharan Raman, and Steve Semancik</i>	463
The Analytical Chemistry of Drug Monitoring in Athletes <i>Larry D. Bowers</i>	485

Errata

An online log of corrections to *Annual Review of Analytical Chemistry* articles may be found at <http://anchem.annualreviews.org/errata.shtml>